



HAL
open science

Structural and mechanistic basis for RiPP epimerization by a radical SAM enzyme

Xavier Kubiak, Ivan Polsinelli, Leonard Chavas, Cameron Fyfe, Alain Guillot,
Laura Fradale, Clémence Brewee, Stéphane Grimaldi, Guillaume Gerbaud,
Aurélien Thureau, et al.

► **To cite this version:**

Xavier Kubiak, Ivan Polsinelli, Leonard Chavas, Cameron Fyfe, Alain Guillot, et al.. Structural and mechanistic basis for RiPP epimerization by a radical SAM enzyme. *Nature Chemical Biology*, In press, 10.1038/s41589-023-01493-1 . hal-04371487

HAL Id: hal-04371487

<https://hal.science/hal-04371487v1>

Submitted on 16 Feb 2024

HAL is a multi-disciplinary open access archive for the deposit and dissemination of scientific research documents, whether they are published or not. The documents may come from teaching and research institutions in France or abroad, or from public or private research centers.

L'archive ouverte pluridisciplinaire **HAL**, est destinée au dépôt et à la diffusion de documents scientifiques de niveau recherche, publiés ou non, émanant des établissements d'enseignement et de recherche français ou étrangers, des laboratoires publics ou privés.



Distributed under a Creative Commons Attribution - NonCommercial - NoDerivatives 4.0
International License

1 **Editor summary:**

2 Peptide epimerization is a common but enigmatic post-translational modification
3 found in antibiotics formed from ribosomally-synthesized and post-
4 translationally modified peptides. Now, crystallographic snapshots,
5 spectroscopy and biochemical investigations, have provided insight into the
6 mechanism of peptide epimerization catalyzed by radical SAM epimerases.

7
8

9 **Peer Review Information:**

10

11 *Nature Chemical Biology* thanks Qi Zhang and the other, anonymous reviewers
12 for their contribution to the peer review of this work.

13
14
15
16
17
18

1. Extended Data

Figure or Table #	Figure/Table title	Filename	Figure/Table Legend
Please group Extended Data items by type, in sequential order. Total number of items (Figs. + Tables) must not exceed 10.	One sentence only	Whole original file name including extension. i.e.: Smith_ED_Fig1.jpg	If you are citing a reference for the first time in these legends, please include all new references in the main text Methods References section, and carry on the numbering from the main References section of the paper. If your paper does not have a Methods section, include all new references at the end of the main Reference list.
Extended Data Fig. 1	Topology diagram of EpeE, radical SAM binding motifs and coordination of SAM in EpeE and representative members of the radical SAM enzyme superfamily.	ED_Figure1.jpg	a , EpeE topology diagram showing a truncated $\alpha 5/\beta 6$ TIM barrel in the radical SAM domain and T-SPASM domain with a single AuxI cluster. The binding region is depicted in bold line. The position of the [4Fe-4S] clusters (yellow and orange) and the coordinating cysteine residues (yellow) are indicated. b , Radical SAM cluster of EpeE in interaction with SAH. Residues from the conserved: GGE, GXIXGXXE, ribose, $\beta 6$ and CX ₃ CX Φ C motifs are colored according to their domain in EpeE (radical SAM domain). The unusual His-20 residue from the CX ₃ CX Φ C motif is highlighted. Hydrogen-bonds are shown with black lines, radical SAM [4Fe-4S] cluster with yellow and orange sticks and SAH with green sticks. c , The CX ₃ CX Φ C motif of structurally characterized members of the radical SAM superfamily of enzymes. The Φ residue is: Tyr in AnSME (green sticks) and CteB (brown sticks); Phe in SkfB (yellow sticks) and SuiB (violet sticks); Met

			in NosL (white sticks). As for CteB, the side chain of the Φ amino acid coordinates both the adenine and the ribose moiety, but only EpeE makes two H-bonds with the N6 and N7 of the adenine moiety.
Extended Data Fig. 2	Interactions stabilizing the T-SPASM domain and the bridging region of EpeE.	ED_Figure2.jpg	a , Overall structure of EpeE highlighting the bridging region (red cartoon) between EpeE domains (radical SAM domain in light blue, T-SPASM in teal). b , The bridging region (red cartoon) makes extensive H-bonds (black dotted lines) with $\alpha 3'$ helix and $\alpha 3'$ - $\alpha 4'$ loop (green cartoon) (left panel). The C-terminal helix $\alpha 5'$ is stabilized by $\alpha 3'$ helix through H-bond and hydrophobic interactions (right panel). c , Comparison between the twitch and SPASM-domains of representative radical SAM enzymes. Similarly to twitch radical SAM enzymes (SkfB & BtrN), EpeE coordinates a single [4Fe-4S] cluster, however, the bridging region extends toward the location of AuxII cluster found in SPASM enzymes (AnSME, CteB & SuiB). The C-terminal $\alpha 5'$ helix of EpeE, absent in twitch-domains, is displaced at the opposite side of the AuxI cluster compared to the C-terminal $\alpha 6'$ helix of SPASM-domain enzymes AnSME and CteB which lies against the $\alpha 6$ helix of the TIM barrel (missing in EpeE). Only the AuxI cluster, $\beta 1'$ - $\beta 2'$ anti-parallel sheets and $\alpha 2'$ helix positions are conserved in all enzymes. The TIM barrel domain is colored in white. The Twitch/SPASM domains are colored by protein. The AuxI and II clusters are shown in yellow and orange sticks.
Extended Data Fig. 3	EPR, UV-visible and HYSORE analysis of EpeE in absence or presence of SAM.	ED_Figure3.jpg	a , Temperature dependence of EPR spectra of dithionite-reduced reconstituted samples of wild-type EpeE in the absence (left panel) or in the presence (right panel) of a 5-fold stoichiometric excess of SAM. The microwave power was adjusted at each temperature to avoid saturation effects. Spectra have been amplitude-normalized. Number of accumulations: 4. The signal of the SAM-bound [4Fe-4S] ⁺ cluster relaxes significantly faster than the one detected in the unbound form. Indeed, the former broadens at temperatures above 6 K and is no longer visible at 30 K and above (right panel) whereas the latter is still detected without significant broadening at 30 K (left panel). Such differences in the relaxation behavior of the two forms allowed us to reveal partial conversion between these forms upon addition of SAM. Indeed, a weak contribution of the unbound form is detected in the sample incubated with a 5-fold excess of SAM when measured at 30 K (right panel). b , Power saturation experiments of dithionite-reduced reconstituted samples of wild-type EpeE in

			<p>the absence (upper panel) or in the presence (lower panel) of a 5-fold stoichiometric excess of SAM. Peak-to-peak amplitudes between features measured as indicated by arrows on left spectra are plotted against square root of microwave power in a log-log plot (blue filled circles). The dotted line represents the non-saturation regime for which the EPR amplitude is proportional to the square root of the microwave power. Other experimental conditions: temperature, 15 K (upper panel) or 6 K (lower panel), microwave power, 0.1 mW (left spectra), number of accumulations, 4. c, UV visible analysis of EpeE wild-type (upper panel) and A3-mutant (lower panel). Before (grey line) and after (black line) anaerobic FeS cluster reconstitution. d, X-band HYSCORE spectra of dithionite-reduced reconstituted samples of wild-type EpeE in the presence (upper panel) or in the absence (lower panel) of a 5-fold stoichiometric excess of SAM. Only the low frequency region is shown. Experimental conditions are given in the Methods section. The low frequency region of the HYSCORE spectrum of the anaerobically reduced and reconstituted wild type enzyme in the presence of SAM displays a complex set of signals in both the (+, +) and (-, +) quadrants which can be unambiguously assigned to a hyperfine coupling to a ^{14}N nucleus in the intermediate coupling regime for which the isotropic part of the hyperfine coupling constant a_{iso} is nearly equal to twice the ^{14}N Larmor frequency, i.e. $\nu_l(^{14}\text{N}) \approx 1.1$ MHz (upper panel). These signals are absent in the corresponding HYSCORE spectrum of the enzyme prepared in the same conditions but without SAM (lower panel).</p>
Extended Data Fig. 4	LC-MS analysis of EpeE incubated with peptides 4, 5, 6 & 7.	ED_Figure4.jpg	<p>Activity of EpeE with peptide 4 (a), 5 (b), 6 (c) and 7 (d) was assayed in deuterated buffer. LC-MS analysis of peptide at T0 (upper left panel) and after 90 min incubation under anaerobic conditions (lower left panel). Comparison between the mass spectrum of the substrate (upper middle panel) and the product (lower middle panel) showed a +1 Da mass increment, consistent with ^2H-atom incorporation while mass spectrum analysis of the 5'-dA is shown in right panel.</p>
Extended Data Fig. 5	LC-MS/MS analysis of the peptide 4, 5, 6 and 7 and the reaction products formed after	ED_Figure5.jpg	<p>a, Mass fragmentation spectrum of peptide 4 (upper panel) and the epimerized peptide product (lower panel). (<i>see Supplementary Tables 1 - 2 for full assignment</i>). b, Mass fragmentation spectrum of peptide 5 (upper panel) and the epimerized peptide product (lower panel). (<i>see Supplementary Tables 3 - 4 for full assignment</i>). c, Mass fragmentation</p>

	incubation with EpeE.		spectrum of peptide 6 (upper panel) and the epimerized peptide product (lower panel). (<i>see Supplementary Tables 5 - 6 for full assignment</i>). d , Mass fragmentation spectrum of peptide 7 (upper panel) and the epimerized peptide product (lower panel). (<i>see Supplementary Tables 7 - 8 for full assignment</i>). The relevant ions with a mass shift of +1 Da due to ² H incorporation after reaction with EpeE are highlighted.
Extended Data Fig. 6	Comparison between substrate-free and peptide-bound structures of EpeE.	ED_Figure6.jpg	a , Superimposition of substrate-free and peptide-bound structures of EpeE. b , Close-up view showing the major structural movements including the $\alpha 3'$ - $\alpha 5'$ helices (indicated by arrows in panel a) of the SPASM-related domain. The substrate-free EpeE structure is shown in grey and the peptide-bound EpeE structure in pale cyan (chain A) and deep teal (chain B). Alignment of the substrate-free and -bound structures using all domains (634 residues) has a r.m.s.d. of 0.78 Å, as calculated using Coot SSM.
Extended Data Fig. 7	Peptide 5 bound in the active-site of wild-type EpeE structure.	ED_Figure7.jpg	a , The peptide 5 was built for 7 out of 11 residues (KENRWIL) according to the electron density. The omit map (blue mesh) of peptide 5 (in pink sticks) is contoured at 3 σ . SAH is depicted in stick, the radical SAM [4Fe-4S] and AuxI clusters are shown as spheres. b , Peptide 5 fold. The peptide is shown in salmon (chain C) and orange (chain D) and colored by atom type. Intramolecular interactions are depicted in black dashed line.
Extended Data Fig. 8	Structures of C223A EpeE mutant bound with peptide 5 and 6.	ED_Figure8.jpg	a , Superimposition of EpeE WT in complex with peptide 5 (pale cyan) and EpeE C223A in complex with peptide 5 (bright orange; r.m.s.d. of 0.22 Å). b , Superimposition of EpeE WT in complex with peptide 5 (pale cyan) and EpeE C223A in complex with peptide 6 (green; r.m.s.d. of 0.23 Å). c , Close-up of EpeE C223A mutant active site. The peptide 5 (left panel) was built for 9 out of 11 residues (KSKENRWIL) according to the electron density. The peptide 6 (right panel) was built for all the 11 residues (KENRWILGSGH) according to the electron density. The omit maps (blue mesh) of peptide 5 (pink sticks) and 6 (purple sticks) are contoured at 3 σ . SAH (green) is depicted in stick, the radical SAM [4Fe-4S] and AuxI clusters are shown as spheres. d , Structure of EpeE C223A mutant with peptide 6 in its active site. K171 and D143 are

			stacking H49 from peptide 6 (left panel) while, in the substrate-free WT EpeE structure, D143 and K171 have a distinct orientation stabilized by a salt bridge (right panel). e , The presence of H49 in the structure of EpeE C223A mutant with peptide 6 provided inter-chain interactions between the two enzyme subunits.
Extended Data Fig. 9	The C223 residue in the structures of wild-type EpeE and D210A mutant.	ED_Figure9.jpg	a , Interactions involving D210 in the structure of EpeE with peptide 5. D210 provides key electrostatic interactions to the substrate (residues N41 and R42) and is stabilized by a polar bond with the protein residue T5. The distance between C223 and D210 is 5.08 Å. b , Orientations of C223 in the structure of the D210A EpeE mutant. The omit map (blue mesh) of C223 in chain A (left panel) and chain B (right panel) is contoured at 3σ. C223 was modeled as a persulfurated cysteine residue. In chain A (left panel), C223 adopted two orientations.
Extended Data Table. 1	Crystallographic data and refinement statistics	Table_1.pdf	

19

20

21 1. Supplementary Information:

22 A. PDF Files

23

Item	Present?	Filename	A brief, numerical description of file contents.
		Whole original file name including extension. i.e.: Smith_SI.pdf. The extension must be .pdf	i.e.: <i>Supplementary Figures 1-4, Supplementary Discussion, and Supplementary Tables 1-4.</i>
Supplementary Information	Yes	Supplementary_Information.pdf	Supplementary Tables 1-10

Reporting Summary	Yes	nr-reporting-summary.pdf
Peer Review Information	No	OFFICE USE ONLY

24

25 2. Source Data

26

Parent Figure or Table	Filename	Data description
	Whole original file name including extension. i.e.: <i>Smith_SourceData_Fig1.xls</i> , or <i>Smith_Unmodified_Gels_Fig1.pdf</i>	i.e.: Unprocessed western Blots and/or gels, Statistical Source Data, etc.
Source Data Fig. 4	Source_data_file.csv	Statistical source data for Fig. 4b

27

28

29 Structural and mechanistic basis for RiPP epimerization by 30 a radical SAM enzyme

31

32 **Xavier Kubiak¹⁺, Ivan Polsinelli¹⁺, Leonard M. G. Chavas³⁺, Cameron D Fyfe¹⁺,**
33 **Alain Guillot¹, Laura Fradale¹, Clemence Brewee¹, Stéphane Grimaldi⁴,**
34 **Guillaume Gerbaud⁴, Aurélien Thureau², Pierre Legrand², Olivier Berteau^{1*} &**
35 **Alhosna Benjdia^{1*}**

36 ¹Université Paris-Saclay, INRAE, AgroParisTech, Micalis Institute, ChemSyBio, 78350
37 Jouy-en-Josas, France

38 ²Synchrotron SOLEIL, HelioBio group, L'Orme des Merisiers, 91190 Gif sur-Yvette,
39 France

40 ³Nagoya University, Nagoya 464-8603, Japan.

41 ⁴Aix Marseille Univ, CNRS, BIP, IM2B, IMM, Marseille, France

42

43 *Corresponding authors. Email: Olivier.Berteau@inrae.fr; Alhosna.Benjdia@inrae.fr

44 ⁺Equal contribution

45 **D-amino acid residues have been reported in countless peptides and natural products**
46 **including ribosomally-synthesized and post-translationally modified peptides (RiPPs),**
47 **where they are critical for the bioactivity of several antibiotics and toxins. Recently,**
48 **radical S-adenosyl-L-methionine (SAM) enzymes have emerged as the only biocatalysts**

49 capable of installing direct and irreversible epimerization in RiPPs. However, the
50 mechanism underpinning this biochemical process is ill-understood and the structural
51 basis for this post-translational modification remains unknown. Here we report an
52 atomic-resolution crystal structure of a radical SAM RiPP-modifying enzyme in complex
53 with its substrate properly positioned in the active site. Crystallographic snapshots,
54 SEC-SAXS, EPR spectroscopy and biochemical analyses revealed how epimerizations
55 are installed in RiPPs and support a unprecedented enzyme mechanism for peptide
56 epimerization. Collectively, our study brings unique perspectives on how radical SAM
57 enzymes interact with RiPPs and catalyze post-translational modifications in natural
58 products.

59 Introduction

60 Ribosomally-synthesized and post-translationally modified peptides (RiPPs) form one of the
61 major families of natural products^{1,2}. They have recently attracted considerable interest
62 because of their involvement in the homeostasis of the human microbiota²⁻⁶ and their potential
63 to develop innovative antibiotics⁷⁻⁹. The biosynthesis of RiPPs usually follows a simple logic
64 with the translation of a precursor peptide containing a leader or a follower sequence² which
65 is recognized by tailoring enzymes *via* a specific domain called RRE (RiPP precursor peptide
66 recognition element)¹⁰. After modification, the leader sequence is cleaved off and the modified
67 peptide secreted. If the general principles are well established, how post-translational
68 modifications are installed and precursor peptides recognized by biosynthetic machineries
69 remains largely elusive^{1,2}.

70 Among the broad diversity of RiPP post-translational modifications, epimerization has been
71 only marginally investigated. In eukaryotes, the L-to-D conversion of peptide residues is critical
72 for the activity of various toxins, venoms and neuro-peptides¹¹. However, the catalytic
73 processes underpinning these transformations are largely unknown. In prokaryotes, the
74 combined action of a dehydratase and a reductase has been shown to result in the conversion
75 of L-Ser and L-Thr into D-Ala and D- α -aminobutyrate, respectively^{12,13}. However, not only this
76 transformation is restricted to Ser and Thr residues but it leads to the modification of the nature
77 and reactivity of the amino acid side-chain.

78 Recently, novel RiPP families including proteusins¹⁴ and eipeptides⁹ have been shown to
79 contain D-amino acid residues formed by the direct and irreversible epimerization of L-
80 residues^{2,9,14,15}. *In vivo* and *in vitro* studies have demonstrated that eipeptides induce the
81 expression of LiaRS, a two-component system that orchestrates the cell envelope stress
82 response in *Bacillus subtilis*¹⁶⁻¹⁸. This system, highly conserved among Firmicutes, regulates
83 the expression of various genes involved in oxidative stress and cell wall antibiotic responses¹⁷⁻
84 ¹⁹. We have shown that the activity of eipeptides is strictly dependent on the presence of
85 epimerized residues⁹ (**Figs. 1a, b**) and established that they have a distinct mode of action
86 compared to other known antimicrobial peptides¹⁸. In addition, we have demonstrated that
87 eipeptides are widely distributed in the human microbiota^{9,17,18} and that epimerizations are
88 catalyzed by a radical S-adenosyl-L-methionine (SAM or AdoMet) enzyme called EpeE^{9,17}.
89 Radical SAM enzymes are central biocatalysts in RiPPs biosynthesis and have been shown
90 to install an outstanding diversity of post-translational modifications^{4,5,8,20-26}. However, until
91 now, no radical SAM enzyme has been crystallized in complex with its peptide substrate
92 properly positioned in the active site, limiting our understanding of their catalysis.

93 To decipher how radical SAM enzymes introduce post-translational modifications in RiPPs and
94 catalyze epimerization, we have performed EPR, SEC-SAXS and structural analysis of the
95 radical SAM epimerase EpeE from *B. subtilis*^{9,17}. We circumvented the intrinsic difficulty to
96 obtain RiPP-enzyme complexes by developing a RiPP-fragment based approach combined
97 with targeted mutagenesis. This novel approach allowed to get at a high resolution, the first
98 crystal structure of a RiPP-modifying radical SAM enzyme in interaction with its substrate. We
99 have also solved the structure of several EpeE mutants and trapped an unexpected adduct on
100 a reactive cysteine residue. Collectively, our work provides a structural and mechanistic
101 rationale for peptide epimerization, a rare case of redox-neutral reaction catalyzed by radical
102 SAM enzymes.

103

104 Results

105 EpeE, a RiPP radical SAM enzyme with a truncated TIM barrel

106 We crystallized EpeE anoxically in the presence of the S-adenosyl-L-methionine (SAM) or S-
107 adenosylhomocysteine (SAH) cofactor. No significant structural difference was measured
108 (r.m.s.d value of 0.293 Å) however, in subsequent experiments SAH gave high-resolution
109 structures when co-crystallization was performed with peptide substrates. The structure of
110 EpeE with SAH, featuring a homodimer in the asymmetric unit, was determined at resolution
111 of 2.4 Å (**Fig. 1c**). Out of the 319 protein residues, electron density was observed for residues
112 1 to 317 in both chains. EpeE exhibits several unique features: first, it is built on a truncated
113 radical SAM domain consisting of an N-terminal partial triose-phosphate isomerase (TIM)
114 barrel fold (*i.e.* $\beta 6/\alpha 5$) instead of the canonical (β/α)₆ TIM barrel. Only the radical SAM
115 enzymes QueE²⁷ and BtrN²⁸, which modify small organic substrates, exhibit a shorter core
116 domain (*i.e.* a $\beta 6/\alpha 3$ and $\beta 5/\alpha 4$ partial TIM barrel, respectively). Second, EpeE is devoid of the
117 $\alpha 4a$ helix connecting $\beta 4$ -sheet to $\alpha 4$ -helix and found in all structurally characterized RiPP-
118 modifying radical SAM enzymes^{29,30} (**Extended Data Fig. 1a**). Among the radical SAM motifs,
119 we identified the three cysteine residues (C14, C18 and C21) as coordinating the radical SAM
120 [4Fe-4S] cluster with SAH bound, as expected, to the unique iron-atom through its carboxy
121 and amino groups (**Fig. 1d**). The SAH ligand was further stabilized by the conserved GGE,
122 ribose, “GXIXGXXE” and $\beta 6$ motifs (**Extended Data Fig. 1b**)³¹. However, in the CX₃CX Φ C
123 motif, the Φ residue is not an aromatic residue but H20 which coordinates both N6 and N7
124 from the adenine moiety and unexpectedly stabilizes the ribose moiety *via* side-chain H-bond
125 with O2' (**Extended Data Fig. 1b-c**). Finally, the GGE motif also contains a non-proline *Cis*-
126 peptide bond between the two glycine residues.

127 A C-terminal domain with an unusual architecture

128 As a hallmark, radical SAM enzymes involved in peptide or protein post-translational
129 modifications have been shown to possess a C-terminal domain housing additional iron-sulfur
130 clusters. This C-terminal domain is either between 106-115 residues long with two auxiliary
131 iron-sulfur clusters and called a SPASM domain^{29,30,32,33}, or significantly shorter and
132 unstructured with a single iron-sulfur cluster and called a twitch domain³⁴. Single anomalous
133 diffraction at the peak absorption wavelength of iron was consistent with the presence of four
134 iron-sulfur clusters in the EpeE dimer (**Extended Data Table 1**). Besides the radical SAM [4Fe-
135 4S] cluster, a single auxiliary cluster (AuxI), best accounted for by a [4Fe-4S] cluster and fully
136 ligated by four cysteine residues (C206, C222, C289 and C292) was identified (**Fig. 1d**). Two
137 of these 4 cysteine ligands are flanking the conserved β -hairpin while the other two are
138 localized in the $\alpha 4'$ helix. This iron-sulfur cluster, located at 16.9 Å from the radical SAM cluster,
139 belongs to the C-terminal domain which overall length (111 residues) unexpectedly exceeds
140 the size of a twitch domain. In addition, the $\beta 6$ - $\beta 1'$ bridging loop makes extensive H-bond
141 interactions with the $\alpha 3'$ helix and the $\alpha 3'$ - $\alpha 4'$ loop and extends toward the location where the
142 second cluster is found in SPASM domains (**Extended Data Fig. 2**)³⁵. Additional helices ($\alpha 3'$,
143 $\alpha 4'$, $\alpha 5'$), absent in twitch domains and involving a tight H-bond network, π - π stacking and
144 hydrophobic interactions, are also present establishing a unique and high secondary structure
145 organization (**Extended Data Fig. 1a, 2**). Overall, the EpeE structure blurs the demarcation
146 between SPASM and twitch domains and defines a transient architecture that we propose to
147 call a T-SPASM domain.

148

149 EPR spectroscopic characterization of EpeE

150 To investigate the properties of the two iron-sulfur clusters, we analyzed EpeE by EPR
151 spectroscopy. The EPR spectrum of EpeE, after reconstitution and reduction, showed a single
152 paramagnetic component characterized by an axial shape with g -values $g_{\parallel} = 2.036$ and $g_{\perp} =$
153 1.929 , which are typical for a reduced $S = \frac{1}{2}$ radical SAM $[4\text{Fe-4S}]^+$ cluster (**Fig. 1e**, trace 1)³⁶.
154 The signal displayed significant relaxation broadening at temperatures above 30 K when
155 recorded under non-saturating microwave power (**Extended Data Fig. 3a, b**). Consistent with
156 this assignment, it disappeared in the A3-mutant, in which the three cysteines coordinating the
157 radical SAM cluster have been substituted by alanines (**Fig. 1e**, trace 3). Iron-sulfur
158 determination indicated that, in agreement with its UV-visible spectrum, the reconstituted wild-
159 type EpeE contained 8.6 ± 0.5 mol of Fe per mole of protein whereas the A3-mutant contained
160 $4.8 \text{ mol} \pm 0.13$ of Fe per mole of protein (**Extended Data Fig. 3c**). This supports the presence
161 of two and one $[4\text{Fe-4S}]$ cluster in the wild-type and A3-mutant, respectively. Therefore, the
162 absence of any other signal in the reduced wild-type or A3-mutant is consistent with the fact
163 that the auxiliary cluster is in the EPR silent $[4\text{Fe-4S}]^{2+}$ redox state, most probably because of
164 its very low redox potential as reported for other radical SAM enzymes^{37,38}. The addition of
165 SAM to the dithionite-reduced wild-type enzyme induced a substantial change in the
166 resonance position and shape of the EPR spectrum. Notably, a signal from an $S = \frac{1}{2}$
167 paramagnetic species having all g -values smaller than 2.00 (*i.e.* $g_{1,2,3} = (1.983, 1.871, 1.790)$)
168 was detected, as shown in the spectrum measured at 6 K under non-saturating conditions
169 (**Fig. 1e**, trace 4 & **Extended Data Fig. 3a, b**). Absent from the A3-mutant (**Fig. 1e**, trace 6),
170 this signal is assigned to a SAM-bound form of the radical SAM $[4\text{Fe-4S}]^+$ cluster. Radical SAM
171 $[4\text{Fe-4S}]^+$ clusters having all g -values smaller than 2.0 have been reported for other
172 enzymes^{33,39,40} and generally associated with a cluster form in which SAM binds to the unique
173 iron of cluster, an assignment further supported by HYSCORE measurements (**Extended Data**
174 **Fig. 3d**).

175 **Structure of EpeE in complex with a peptide substrate**

176 Initial attempts to crystallize EpeE with its full-length substrate failed, as commonly
177 encountered with RiPP-modifying enzymes. This recurrent failure likely results because of the
178 intrinsically disordered nature of peptides and the fact that many RiPP-modifying enzymes
179 have relaxed substrate specificity, essential to introduce post-translational modifications at
180 distinct sites⁴¹. Indeed, EpeE like other radical SAM enzymes^{15,42} introduces multiple post-
181 translational modifications and must thus adapt to different peptide contexts. To circumvent
182 this inherent difficulty, we designed a peptide library covering the leader and core sequence of
183 the peptide substrate EpeX 1 (**Fig. 2a**). This RiPP-fragment library was assayed for activity
184 and co-crystallization with EpeE. All peptides containing the core sequence (peptides 4-7)
185 proved to be substrates as shown by labeling experiments performed in deuterated buffer
186 (**Extended Data Fig. 4, 5 and Supplementary Tables 1-8**)^{9,15,43}. LC-MS/MS analysis notably
187 confirmed that ²H-atom incorporation occurred exclusively at the expected epimerization sites.
188 Of note, with peptides 4 and 7, we monitored significant uncoupling between SAM cleavage
189 and epimerization activity, as revealed by 5'-dA isotopic enrichment (**Extended Data Fig. 4a,**
190 **d**). In contrast, with peptides 5 and 6, no solvent ²H-atom was incorporated into 5'-dA,
191 supporting a strict coupling with these substrates (**Extended Data Fig. 4b, c & Extended Data**
192 **Fig. 5**).

193 Remarkably, EpeE co-crystallization assays under anaerobic conditions with SAH and the
194 RiPP-fragment library, led to a high-resolution structure (2.39 Å) of EpeE in complex with
195 peptide 5 (**Fig. 2a & b**). Crystal form in space group $P2_12_12_1$ was identical to the one obtained

196 when crystallizing the substrate-free enzyme, with an asymmetric unit consisting of a
197 homodimer (**Extended Data Table 1**). Only subtle changes mainly located in the T-SPASM
198 domain could be measured between the free- and bound-substrate structures (r.m.s.d of 0.78
199 Å, **Extended Data Fig. 6**). In addition, a strong electron density for the peptide **5** was observed
200 for 7 out of 11 residues (**Extended Data Fig. 7a**). The peptide fits in the open cavity located
201 at the bottom of the partial TIM barrel and binds between the β 1- β 5 of the radical SAM domain
202 and the beginning of the T-SPASM domain (**Fig. 2b**). Peptide **5** is coordinated by a complex
203 network of inter- and intra-molecular interactions folding partially the peptide into a 3_{10} -helix
204 (**Extended Data Fig. 7b**). The residue target of the modification I44 is in the vicinity (3.6 Å) of
205 the aromatic rings of F23 and F228 (**Fig. 2c**). Interestingly C223, which we proposed as the
206 H-atom donor of the reaction⁹, is part of the hydrophobic pocket around I44 and provides key
207 interactions with I44 including a polar contact *via* its backbone oxygen and hydrophobic
208 interactions. I44 is also stabilized through its backbone oxygen by hydrogen bonding with the
209 sidechain oxygen of T57 (**Fig. 2c**). Further stabilization of the substrate is provided by π - π
210 stacking between W43 and the aromatic ring of F175 (EpeE) (π - π centroids 4.6-5.4 Å). Finally,
211 polar interactions with the adenine moiety of SAH (3.28 Å) and hydrophobic contacts with I178
212 and P225 (3.59 Å) are also involved in stabilizing I44 through W43 (**Fig. 2c**). The importance
213 of W43 in peptide stabilization is consistent with the fact that the two epimerization sites (I44
214 and V36), despite lacking sequence homology, are preceded by an aromatic residue. Hence,
215 EpeE appears to recognize a hydrophobic motif for epimerization installation. Further
216 interactions between EpeE and its substrate involve salt bridges between the sidechain of
217 D210 and the sidechains of two substrates residues, R42 and N41, this latter having also a
218 direct interaction with G208 (**Fig. 2c**). The radical SAM domain through S55 and T57 side
219 chains also contributes to peptide stabilization mainly through polar contacts, while T113 and
220 L84 interact with L45 from the peptide through water contacts. Similarly, N147 (β 5) coordinates
221 a water molecule that makes polar contacts with three residues (T43, L45 and R42) from
222 peptide **5** (**Fig. 2c**). Hence, the structure of the complex revealed that the substrate not only
223 interacts with the two protein domains but also with the SAH cofactor. It also surprisingly
224 showed that the substrate residues preceding I44 adopt a 3_{10} -helix secondary structure.

225

226 **Cys223 as a critical H-atom donor**

227 In the enzyme-substrate complex, the distance between the targeted substrate residue I44 C $_{\alpha}$ -
228 atom and the C5'-atom of SAM (3.8 Å) is perfectly suited for direct H-atom abstraction from
229 the substrate. Remarkably, on the opposite side of I44, we found C223 (S_{C223}-C $_{\alpha}$ -I44-C5'_{SAH}
230 angle: 152°) with a sulfur (C223) to C $_{\alpha}$ -atom (I44) distance of 6.3 Å (**Fig. 2d**). Although this
231 distance is too large for direct interaction between C223 and the transient peptide carbon-
232 centered radical formed during catalysis, this distance is likely to shorten due to the loss of I44
233 stereochemistry. In addition, the structure of the D210A mutant (see below) has revealed that
234 C223 can sample other conformations bringing the sulfhydryl group 2 Å closer to the radical
235 SAM [4Fe-4S] cluster. Altogether, these data are in full agreement with the proposed role of
236 C223 as the H-atom donor of the reaction.

237

238 **Crystallographic snapshots of an EpeE active-site mutant**

239 Because of the critical role of C223 in the epimerization reaction, we reasoned that the C223A
240 mutant could provide further stabilization to the transient peptide-protein complex. Structure of
241 this mutant perfectly superimposed with the one of the wild-type enzyme (r.m.s.d. value of
242 0.2945 Å,) with the SAM cofactor in direct interaction with the radical SAM [4Fe-4S] cluster.

243 EPR analysis of this mutant (**Fig. 1e**, traces 2 & 5), in the absence or the presence of SAM,
244 showed identical EPR signatures than the wild-type EpeE, supporting that the electronic
245 structure of the radical SAM [4Fe-4S]⁺ cluster is not affected.

246 Gratifyingly, we solved the structure of the C223A mutant at an atomic resolution with peptide
247 **5** and peptide **6** (1.75 Å and 2.15 Å, respectively) in the presence of SAH. Interactions between
248 peptide **5** and the C223A mutant were overall similar to the wild-type enzyme (r.m.s.d 0.22 Å)
249 (**Figs. 3a and Extended Data Fig. 8**). However, we obtained electron density for two additional
250 *N*-terminal amino acid residues located at the very entrance of the active site and forming an
251 additional turn, pointing toward the exit of the active site (**Fig. 3a and Extended Data Fig. 8c**).

252 The peptide **6**-C223A mutant complex revealed the structure of the full *C*-terminal end of EpeX
253 **1** (**Fig. 3b and Extended Data Fig. 8c**). This final peptide segment is stabilized along three β -
254 sheets from the partial TIM barrel (from β_3 to β_5) and points toward the exit of the active site
255 with the final peptide residue H49 making polar contacts with I144, S145 and D143.
256 Interestingly, D143 and K171 from EpeE are stacking H49 (**Fig. 3b**), while in the complex with
257 peptide **5** (lacking H49) and in the substrate-free structure, D143 and K171 are stabilized by a
258 salt bridge in a distinct orientation (**Extended Data Fig. 8d, e**).

259 The overlapping sequences of peptides **5** and **6** perfectly superimposed, demonstrating the
260 validity of our RiPP-fragment based approach (**Fig. 3c**). Notably, in both complexes, the
261 relative location of I44 within the active site, remains the same. Unexpectedly, the presence of
262 H49 provides further inter-chain interactions between the two enzyme subunits (**Extended**
263 **Data Fig. 8d, e**). Within the homo-dimeric complex, peptide-peptide interactions are thus likely
264 to significantly contribute to stabilize a productive positioning of the substrate. Exploiting these
265 two atomic-resolution structures, we were able to model, based on the visible electron density,
266 the structure of a peptide spanning 13 residues long (**Fig. 3d**). In this model, I44 is part of a
267 folded peptide region as a 3_{10} -helix while the final GSGH motif has an extended conformation.
268 Remarkably, hydrophobic side-chains are protruding (I44, W43) and alternating with charged
269 residues (E40, R42), reminiscent of the structure of α -helical antimicrobial peptides⁴⁴.

270

271 **Structural basis for RiPP epimerization**

272 As shown, in all the peptide-enzyme complexes obtained, I44 is perfectly positioned for C α H-
273 atom abstraction (**Fig. 4a**) and formation of a carbon-centered radical. This transient reaction
274 intermediate is likely to react with the sulfhydryl of C223, leading to epimerization of I44 and
275 the formation of a thiyl radical. With the auxiliary cluster (AuxI) in the vicinity of C223, a
276 consistent function would be as an electron shuttle to the thiyl radical. Only few radical SAM
277 RiPP-modifying enzymes have been spectroscopically characterized^{37,45,46} but for some of
278 them, the auxiliary cluster (AuxI) proved to be a low-potential [4Fe-4S] cluster³⁷. In addition,
279 recent investigations have shown that substrate binding can tune the redox properties of the
280 AuxI cluster, further supporting a role as an electron shuttle⁴⁶. In EpeE, AuxI is likely to fulfill a
281 similar function with two tyrosine residues (Y209 and Y2) located beneath the cluster and
282 stabilized by main chain interactions, hydrogen bonds and π - π stacking, ideally positioned to
283 serve as an electron conduit from the protein surface (**Fig. 4a**). In addition, we also identified
284 in the immediate environment of C223, only one titratable residue: D210. This residue provides
285 key electrostatic interactions to the substrate (**Figs. 2c, 3a and 3b**) and is stabilized by a polar
286 bond with T5 (**Extended Data Fig. 9a**).

287 To probe for the function of these residues, we generated several mutants by substituting the
288 two tyrosines with phenylalanine residues (Y2F-Y209F mutant) and by replacing D210 with an

alanine residue (D210A mutant). The activity of these mutants was assayed using peptide **6** as substrate and a physiological reducing system (NADPH/flavodoxin/flavodoxin reductase). As shown, we obtained a tight coupling between SAM cleavage (5'-dA production) and peptide epimerization with the wild-type enzyme (**Fig. 4b**). In contrast, with the C223A mutant, epimerization was strongly impaired while SAM cleavage activity remained similar to the wild-type enzyme. Hence, with the C223A mutant, only the epimerization reaction is affected. The two other mutants Y2F-Y209F and D210A had similar activities compared to the wild-type EpeE (**Fig. 4b**). However, under *in vitro* conditions, the physiological roles of these amino acid residues might be difficult to evidence because of the excess of reductant and electrons present in the reaction mixtures.

The high-resolution structure of the D210A mutant in complex with SAH (1.95 Å) was similar to the wild-type enzyme (r.m.s.d. of 0.25 Å). However, it exhibited two major differences: first, C223 adopted a distinct orientation bringing the sulfhydryl group 2 Å closer toward the SAH cofactor. Second, we noted the presence on C223 of an additional electron density (**Extended Data Fig. 9b**). This extra electron density was modeled, after analysis of the $2F_o - F_c$ map maximum intensity, as a second sulfhydryl group (**Extended Data Fig. 9b**). The presence of a persulfur on a reactive cysteine has been reported in several systems including cytochrome thiosulfate dehydrogenase⁴⁷ or the cysteine desulfurase NifS⁴⁸. In the D210A mutant, the origin of this additional sulfur atom is unknown but it supports that C223 is a reactive residue. Careful analysis of all structures showed that this adduct and this sidechain orientation were only present in the D210A mutant, supporting that D210 plays an important role to stabilize C223. Finally, polar contacts between D210 and T5 sidechains are also reminiscent of the catalytic “acid-alcohol pair” found in cytochrome P450⁴⁹ and involved in proton transfer within the active site. Collectively, these data support that D210 interacts with C223 and could play an important role not only in substrate stabilization and positioning, but also for C223 reactivity.

Discussion

Despite major advances in our understanding of RiPP biosynthesis, core peptide recognition by RiPP enzyme active sites is largely unknown. These enzymes must often recognize multiple modification sites to generate their final products, supporting a relaxed substrate specificity. Recent studies have shown that RiPP-modifying enzymes including radical SAM enzymes, while catalyzing a vast array of chemical transformations^{1,2}, share conserved structural features such as an RRE to interact with the leader peptide¹⁰ and ensure the fidelity of the post-translational modifications. However, this structural element is absent from many enzymes questioning the processes underpinning their specificity.

To address these fundamental questions, we have investigated the radical SAM epimerase EpeE⁹ alone and in complex with several peptide substrates. Structural and EPR analyses demonstrate that EpeE contains two [4Fe-4S] clusters and has an unusual architecture. Its compact fold markedly differs from all known RiPP-modifying radical SAM enzymes by the notable absence of an RRE domain and of the α_6 and α_{4a} helices from the partial TIM barrel. In addition, EpeE possesses a unique C-terminal domain which shares the single [4Fe-4S] cluster of twitch-domains but with an overall fold reminiscent of the SPASM-domain, that we propose to call a T-SPASM domain (**Figs. 1 & 2**).

By generating a RiPP-fragment library, we were able to obtain high-resolution crystallographic snapshots of a RiPP-modifying radical SAM enzyme in a pre-catalytic state (**Figs. 2b, c and**

334 **Extended Data Fig. 8**) with its substrate properly located in the active site. Currently, only two
335 structures of radical SAM enzymes catalyzing RiPP post-translational modifications have been
336 solved in complex with peptide substrates^{29,30}. Intriguingly, in SuiB, which catalyzes the
337 formation of carbon-carbon bonds, the leader peptide was found in the partial TIM barrel
338 instead of the RRE and no electron density was present for the core peptide. For CteB which
339 catalyzes thioether bond formation, only the leader peptide sequence and the first three
340 residues of the core region were visible in the co-crystallized structure³⁰.

341 In sharp contrast, the structures of EpeE and its C223A mutant in complex with different
342 peptide substrates revealed that I44, the amino acid residue target of the modification, is in an
343 ideal position for direct C_α H-atom abstraction by the 5'-dA radical (I44 C_α-atom-C5' distance
344 of 3.8 Å). Structural analysis also revealed that a conserved cysteine residue (C223) is located
345 beneath I44 to serve as an H-atom donor. By using a physiological reductant system, we
346 demonstrated that while the SAM cleavage activity is not affected by mutation of C223, the
347 second part of the reaction (*i.e.* H-atom transfer to the carbon-centered radical) is hampered
348 leading to a strong uncoupling between SAM cleavage and peptide epimerization (**Fig. 4b**).
349 Interestingly, while the distance in the peptide-enzyme complex is too long (6.3 Å, **Fig. 2d**) for
350 a direct interaction between C223 and the C_α-atom of I44, structural analysis of the D210A
351 mutant revealed that C223 can sample various conformations, bringing the sulfur atom closer
352 to the I44 C_α-atom. Altogether, these results support that radical SAM peptide epimerases
353 effectively use a cysteine residue as critical H-atom donor, a strategy likely common to all
354 radical SAM epimerases^{15,50,51}.

355 Another advantage of our RiPP-fragment based approach was to gain structural information
356 regarding RiPP structure during catalysis. Indeed, based on the structure of several peptide-
357 enzyme complexes, we were able to model up to 13 substrate residues, starting from the
358 residue after V36 up to the C-terminal end of EpeX. This model reveals that EpeX is partially
359 folded as a 3₁₀-helix in the enzyme active site with protruding hydrophobic side-chains.
360 Although 3₁₀-helices have been identified in other RiPPs, the core region is usually
361 unstructured or with a U-turn shape in RiPP-enzyme complexes⁵²⁻⁵⁵.

362 In sharp contrast to the known structures of (non-radical SAM) RiPP-modifying enzymes⁵²⁻⁵⁵,
363 only minor rearrangements occurred in EpeE upon substrate binding. Peptide-enzyme
364 interactions are driven not only by residues from the radical SAM domain but also by residues
365 from the T-SPASM domain and the SAM cofactor itself, forging a complex network of
366 interactions that ensure substrate recognition in the absence of RRE. Interestingly, a similar
367 strategy implying interactions between the substrate backbone with the protein domains and
368 the SAM cofactor, has been recently reported for the B₁₂-dependent radical SAM enzyme
369 Mmp10⁵⁶.

370 Another intriguing finding of this study is that with peptide **6**, not only the full C-terminal end of
371 eptideptide could be accommodated in the EpeE dimer without steric clashes but unexpectedly,
372 further stabilization was provided by the last residue. Indeed, H49, stacked between K171 and
373 D143, directly interacts through inter-chain interactions with H49 from the second subunit
374 (**Extended Data Fig. 8d, e**), supporting a physiological role for the dimer (**Fig. 5a**). To validate
375 this model, we performed anaerobic SEC-SAXS analysis in order to determine the
376 oligomerization state of EpeE in solution. SEC-SAXS analysis showed that anaerobically
377 reconstituted EpeE in the presence of SAM behaved as a homogenous globular and folded
378 protein (**Fig. 5b**) with a radius of gyration of 28.7 Å and an estimated molecular weight of 73-
379 71 kDa. These experimental data are consistent with EpeE being exclusively a dimer in

380 solution and are in full agreement with our structural analysis. Additionally, surface interaction
381 calculations using the PDBePISA server⁵⁷ also supported that the dimer is the most stable
382 species (**Supplementary Tables 9-10**). This dimer provides an elegant structural rationale for
383 the installation of the two epimerizations in epeptides. Initially, two peptide molecules interact
384 within the EpeE dimer, positioning I44 in the active site for direct attack by the 5'-dA radical.
385 The presence of a hydrophobic residue before each targeted residue is also likely to provide
386 key stabilization. Following H-atom abstraction, the amino acid configuration is lost (**Fig. 5c**)
387 and the radical substrate intermediate is quenched by C223, which is ideally located on the
388 opposite side of the targeted residue. Similar critical cysteine residues have been identified in
389 all radical SAM epimerases investigated to date^{15,50,51}. After configuration inversion, a transient
390 thiyl radical is generated on C223. D210 which forms a pair with T5 and stabilizes C223, is the
391 only residue that could serve to regenerate the thiyl radical using a proton-coupled electron
392 transfer pathway. Following, the first epimerization event, the dimer progresses toward V36
393 which is already in the vicinity the active site (**Fig. 5a**). In support of this model, not only we
394 have always crystallized peptides with I44 positioned for H-atom abstraction but also I44 was
395 always the hotspot for epimerization (**Extended Data Fig. 4**), suggesting a *C-to-N* directionality
396 in EpeE like in PoyD¹⁵.

397 In conclusion, our study reports an unprecedented binding mode for a RiPP-modifying enzyme
398 and expands the structural diversity of radical SAM enzymes catalyzing RiPP post-translational
399 modifications. Unexpectedly, the EpeE structure reveals that inter-chain interactions could play
400 a significant role for the sequential installation of epimerizations. Finally, this work illuminates
401 how radical SAM enzymes catalyze peptide epimerization, a rare example of redox-neutral
402 reaction, delineating novel reactivity in enzyme active sites.

403 **Acknowledgments**

404 This work was supported by the French National Research Agency (ANR grants: ANR-17-
405 CE11-0014 to O.B.; ANR-20-CE44-0005 to O.B.). The authors are grateful to the EPR facilities
406 available at the French EPR network (IR CNRS 3443, now INFRANALYTICS, FR2054) and
407 the Aix-Marseille University EPR center. We acknowledge SOLEIL (Saint-Aubin, France) for
408 provision of synchrotron radiation facilities and we would like to thank the PROXIMA-1 and
409 SWING staff for assistance in using the beamline.

410

411 **Author contributions**

412 A.B. & O.B. research design and funding acquisition; X.K., I.P., L.M.G.C., C.D.F., A.G., S.G.,
413 G.G., .A.T., P.L., O.B. & A.B performed research; X.K., I.P., L.F. & C.B. protein production.
414 X.K., I.P., L.M.G.C., C.D.F., A.G., S.G., G.G., .A.T., P.L., O.B. & A.B. analyzed data. O.B. &
415 A.B. wrote the manuscript with contributions from co-authors.

416

417 **Competing Interests Statement**

418 The authors declare no competing interests.

419

420 **Additional information**

421 Extended data is available for this paper.

422

423

424

425

Figure legends

426
427
428
429
430
431
432
433
434
435
436
437
438
439
440
441
442
443
444
445

Fig. 1 - Epipeptide biosynthesis and overall structure of the EpeE radical SAM epimerase. **a**, Sequence of EpeX precursor with the leader (white circles) and the core peptide sequence (blue circles) indicated. After modification by EpeE, the mature epipeptide is produced with epimerization of V36 and I44 (in red). **b**, Epimerization reaction catalyzed by EpeE showing the C_α H-atom, target of the modification, in red. **c**, Overall structure of the EpeE homodimer in the asymmetric unit (left panel). Radical SAM domain (light blue, residues 1-175) and T-SPASM domain coordinating the auxiliary (AuxI) [4Fe-4S] cluster (teal, residues 206-317). **d**, Crystal structure of EpeE with bound SAH. The [4Fe-4S] and AuxI clusters are shown as balls and sticks (yellow and orange spheres) and SAH as sticks (green). The omit map (blue mesh) of SAH and [4Fe-4S] clusters are contoured at 3σ. AuxI: auxiliary cluster. **e**, EPR analysis of EpeE. X-band CW EPR spectra of dithionite-reduced reconstituted samples of EpeE WT (traces 1, 4), C223A mutant (traces 2, 5) and **A3**-mutant (traces 3, 6) and in the absence (traces 1-3) and presence (traces 4-6) of an excess of SAM. Experimental conditions: temperature, 15 K (traces 1-3) or 6 K (trace 4-6), microwave power, 0.1 mW, field modulation amplitude, 1 mT, microwave frequency, 9.48 GHz, number of accumulations, 8 (1-3), or 16 (4-6). Protein concentration, 320 μM (1, 4), 223 μM (2, 5), 380 μM (3, 6), SAM concentration, 1 mM.

446
447
448
449
450
451
452
453
454
455
456
457
458
459
460
461
462
463
464
465

Fig. 2 - Structure of EpeE in interaction with a peptide substrate and SAH cofactor. **a**, Sequences of the peptide substrates assayed: EpeX (peptide **1**) and the RiPP-fragments: peptides **2**, **3**, **4**, **5**, **6** & **7**. The leader peptide is shown in white circles and the core peptide is indicated by blue circles. The two residues, targets of the modification by EpeE (*i.e.* V36 and I44) are shown in red in blue circles. **b**, Overall structure of EpeE in complex with the peptide **5** (left panel). The bound peptide **5** (residues K₃₉ENRWIL₄₅) is depicted in pink sticks, SAH is shown in green and the two [4Fe-4S] clusters are in yellow and orange. APBS-derived surface electrostatics of EpeE reveals three distinct electrostatic potentials in the EpeE peptide binding pocket (right panel). Surface colored according to electrostatic potential with positively charged regions in blue and negatively charged regions in red. The bound peptide is shown in pink sticks. **c**, Coordination of the peptide **5** (pink sticks) by both EpeE domains. The binding pocket within 5 Å of the peptide consists of 6 hydrophobic residues (F23, F175, F228, L84, I85, I178), five polar uncharged residues (S55, T57, T83, T113, S224), and three charged residues (N9, N147, D210), in addition to C223, P176 and P225. SAH, the radical SAM [4Fe-4S] and AuxI clusters are shown as sticks. Amino acid residues in light blue belong to the radical SAM domain and the ones in teal are from the T-SPASM domain. **d**, Close-up of the EpeE active site showing SAH in green, the peptide **5** in pink, C223 in teal and the two [4Fe-4S] clusters in yellow and orange. The distances between the C5' atom of SAH and the C_α atom of I44 from peptide **5** (3.8 Å) and between I44 and the sulfur-atom of C223 from EpeE (6.3 Å) are indicated by dashed lines.

466

467
468
469
470
471
472
473

Fig. 3 - Structures of C223A mutant in interaction with two peptide substrates and SAH cofactor. **a**, Close-up of EpeE **C223A** mutant active site showing protein residues from the radical SAM (in light blue) and the T-SPASM (in teal) domains in interaction with the peptide **5** (in pink). Dashed lines show polar contacts between peptide **5** and protein residues. SAH is depicted in green sticks and both [4Fe-4S] clusters are shown in yellow and orange spheres. **b**, Close-up of EpeE **C223A** mutant active site showing protein residues from the radical SAM (in light blue) and the T-SPASM (in teal) domains in interactions with the peptide **6** (in light

474 green). Dashed lines show polar contacts between peptide **6** and protein residues. SAH is
475 depicted in green sticks and both [4Fe-4S] clusters in yellow and orange spheres. The
476 epeptide C-terminal region points toward the exit of the active site with the last residue H49
477 interacting with residues 143-145. **c**, Superimposition of the structures of peptides **5** and **6**
478 obtained from the respective complexes with the **C223A** EpeE mutant. **d**, Model of the 13
479 residues (KSKENRWILGSGH) identified in C223A EpeE mutant active site. The region that
480 holds I44 is folded as a 3_{10} -helix while the C-terminal residues (GSGH) featured an extended
481 conformation.

482

483 **Fig. 4 – Amino acid network in the active site of the radical SAM enzyme EpeE.** **a**, Close-
484 up of EpeE active site with key residues highlighted. Distances are shown as dotted lines with
485 values indicated in Å. **b**, Time-course analysis of epimerized peptide (open and closed
486 squares) and 5'-dA (open and closed diamonds) production by EpeE and mutants (**C223A**,
487 **D210A** & **Y2F/Y209F**) incubated with SAM and peptide **6** under anaerobic and reducing
488 conditions with the flavodoxin/flavodoxin reductase/NADPH system. Experiments were
489 performed in duplicate and analyzed by LC-MS.

490

491 **Fig. 5 – Substrate interaction and proposed mechanism for EpeE.** **a**, Model of
492 epimerization catalyzed by EpeE on the EpeX peptide. In the EpeE dimer, two peptide
493 molecules (EpeX) interact through inter- (H49) and intra-chain interactions with I44 positioned
494 in the active site for an attack by the 5'-dA radical. After the first epimerization event, the dimer
495 progresses toward V36, the second epimerized residue. **b**, SEC-SAXS analysis of EpeE in the
496 presence of SAM (panel 1) or SAM and peptide **6** (panel 2). The UV visible signal at $\lambda = 280$
497 nm (blue) and SAXS intensity at zero angle (red) is superimposed with the computed Rg from
498 SAXS data (open circles). SAXS curves of EpeE in the presence of SAM (panel 3) and EpeE
499 in the presence of SAM and peptide **6** (panel 4). Fit curves using PepsiSAXS are indicated by
500 a red trace and χ^2 value determined between the experimental data and the simulated model
501 (see **Supplementary Table 10**). **c**, Proposed mechanism for EpeE. Following the reduction of
502 the radical SAM cluster, the 5'-dA radical generated, abstracts the C $_{\alpha}$ H-atom of the target
503 residue. The carbon-centered radical formed on the substrate reacts with C223, leading to
504 configuration inversion of I44 and formation of a thiyl radical on C223. The AuxI [4Fe-4S]
505 cluster, likely assisted by D210, is ideally positioned to regenerate C223 through a proton-
506 coupled electron transfer pathway.

References

- 507
508
509 1. Montalban-Lopez, M. et al. New developments in RiPP discovery, enzymology and
510 engineering. *Nat Prod Rep* **38**, 130-239 (2021).
511 2. Benjdia, A. & Berteau, O. Radical SAM Enzymes and Ribosomally-Synthesized and Post-
512 translationally Modified Peptides: A Growing Importance in the Microbiomes. *Front Chem* **9**,
513 678068 (2021).
514 3. Benjdia, A. & Berteau, O. Sulfatases and radical SAM enzymes: emerging themes in
515 glycosaminoglycan metabolism and the human microbiota. *Biochem. Soc. Trans.* **44**, 109-15
516 (2016).
517 4. Balty, C. et al. Ruminococcin C, an anti-clostridial sactipeptide produced by a prominent
518 member of the human microbiota *Ruminococcus gnavus*. *J Biol Chem* (2019).
519 5. Balty, C. et al. Biosynthesis of the sactipeptide Ruminococcin C by the human microbiome:
520 Mechanistic insights into thioether bond formation by radical SAM enzymes. *J Biol Chem* **295**,
521 16665-16677 (2020).
522 6. Balskus, E.P. The Human Microbiome. *ACS Infect. Dis.* **4**, 1-2 (2018).
523 7. Donia, M.S. et al. A systematic analysis of biosynthetic gene clusters in the human microbiome
524 reveals a common family of antibiotics. *Cell* **158**, 1402-14 (2014).
525 8. Benjdia, A., Balty, C. & Berteau, O. Radical SAM Enzymes in the Biosynthesis of Ribosomally
526 Synthesized and Post-translationally Modified Peptides (RiPPs). *Front. Chem.* **5**, 87 (2017).
527 9. Benjdia, A., Guillot, A., Ruffié, P., Leprince, J. & Berteau, O. Post-translational modification
528 of ribosomally synthesized peptides by a radical SAM epimerase in *Bacillus subtilis*. *Nat Chem*
529 **9**, 698-707 (2017).
530 10. Burkhart, B.J., Hudson, G.A., Dunbar, K.L. & Mitchell, D.A. A prevalent peptide-binding
531 domain guides ribosomal natural product biosynthesis. *Nat Chem Biol* **11**, 564-70 (2015).
532 11. Heck, S.D. et al. Posttranslational amino acid epimerization: enzyme-catalyzed isomerization
533 of amino acid residues in peptide chains. *Proc Natl Acad Sci U S A* **93**, 4036-9 (1996).
534 12. Huo, L. & van der Donk, W.A. Discovery and Characterization of Bicereucin, an Unusual d-
535 Amino Acid-Containing Mixed Two-Component Lantibiotic. *J Am Chem Soc* **138**, 5254-7
536 (2016).
537 13. Lohans, C.T., Li, J.L. & Vederas, J.C. Structure and biosynthesis of carnolysin, a homologue of
538 enterococcal cytolysin with D-amino acids. *J Am Chem Soc* **136**, 13150-3 (2014).
539 14. Freeman, M.F. et al. Metagenome mining reveals polytheonamides as posttranslationally
540 modified ribosomal peptides. *Science* **338**, 387-90 (2012).
541 15. Parent, A. et al. Mechanistic Investigations of PoyD, a Radical S-Adenosyl-l-methionine
542 Enzyme Catalyzing Iterative and Directional Epimerizations in Polytheonamide A
543 Biosynthesis. *J Am Chem Soc* **140**, 2469-2477 (2018).
544 16. Butcher, B.G., Lin, Y.P. & Helmann, J.D. The yydFGHIJ operon of *Bacillus subtilis* encodes a
545 peptide that induces the LiaRS two-component system. *J Bacteriol* **189**, 8616-25 (2007).
546 17. Popp, P.F. et al. The Epipeptide Biosynthesis Locus epeXEPAB Is Widely Distributed in
547 Firmicutes and Triggers Intrinsic Cell Envelope Stress. *Microb Physiol*, 1-12 (2021).
548 18. Popp, P.F., Benjdia, A., Strahl, H., Berteau, O. & Mascher, T. The Epipeptide YydF Intrinsically
549 Triggers the Cell Envelope Stress Response of *Bacillus subtilis* and Causes Severe Membrane
550 Perturbations. *Front Microbiol* **11**, 151 (2020).
551 19. Radeck, J. et al. Anatomy of the bacitracin resistance network in *Bacillus subtilis*. *Mol Microbiol*
552 **100**, 607-20 (2016).
553 20. Benjdia, A. et al. The thiostrepton A tryptophan methyltransferase TsrM catalyses a
554 cob(II)alamin-dependent methyl transfer reaction. *Nat. Commun.* **6**, 8377 (2015).
555 21. Pierre, S. et al. Thiostrepton tryptophan methyltransferase expands the chemistry of radical
556 SAM enzymes. *Nat. Chem. Biol.* **8**, 957-9 (2012).
557 22. Parent, A. et al. The B12-radical SAM enzyme PoyC catalyzes valine C-beta-methylation
558 during polytheonamide biosynthesis. *J. Am. Chem. Soc.* **138**, 15515-15518 (2016).
559 23. Freeman, M.F., Helf, M.J., Bhushan, A., Morinaka, B.I. & Piel, J. Seven enzymes create
560 extraordinary molecular complexity in an uncultivated bacterium. *Nat Chem* **9**, 387-395 (2017).

- 561 24. Benjdia, A. et al. Insights into the catalysis of a lysine-tryptophan bond in bacterial peptides by
562 a SPASM domain radical S-adenosylmethionine (SAM) peptide cyclase. *J. Biol. Chem.* **292**,
563 10835-10844 (2017).
- 564 25. Balty, C. et al. Ruminococcin C, an anti-clostridial sactipeptide produced by a prominent
565 member of the human microbiota *Ruminococcus gnavus*. *J Biol Chem* **294**, 14512-14525
566 (2019).
- 567 26. Benjdia, A. et al. Insights into the catalysis of a lysine-tryptophan bond in bacterial peptides by
568 a SPASM domain radical S-adenosylmethionine (SAM) peptide cyclase. *J Biol Chem* **292**,
569 10835-10844 (2017).
- 570 27. Dowling, D.P. et al. Radical SAM enzyme QueE defines a new minimal core fold and metal-
571 dependent mechanism. *Nat Chem Biol* **10**, 106-12 (2014).
- 572 28. Goldman, P.J., Grove, T.L., Booker, S.J. & Drennan, C.L. X-ray analysis of butirosin
573 biosynthetic enzyme BtrN redefines structural motifs for AdoMet radical chemistry. *Proc Natl*
574 *Acad Sci U S A* **110**, 15949-54 (2013).
- 575 29. Davis, K.M. et al. Structures of the peptide-modifying radical SAM enzyme SuiB elucidate the
576 basis of substrate recognition. *Proc Natl Acad Sci U S A* (2017).
- 577 30. Grove, T.L. et al. Structural Insights into Thioether Bond Formation in the Biosynthesis of
578 Sactipeptides. *J. Am. Chem. Soc.* **139**, 11734-11744 (2017).
- 579 31. Vey, J.L. & Drennan, C.L. Structural insights into radical generation by the radical SAM
580 superfamily. *Chem Rev* **111**, 2487-506 (2011).
- 581 32. Haft, D.H. & Basu, M.K. Biological systems discovery in silico: radical S-adenosylmethionine
582 protein families and their target peptides for posttranslational modification. *J. Bacteriol.* **193**,
583 2745-55 (2011).
- 584 33. Benjdia, A. et al. Anaerobic sulfatase-maturing enzyme--a mechanistic link with glyceryl
585 radical-activating enzymes? *FEBS J* **277**, 1906-20 (2010).
- 586 34. Grell, T.A.J. et al. Structural and spectroscopic analyses of the sporulation killing factor
587 biosynthetic enzyme SkfB, a bacterial AdoMet radical sactisynthase. *J. Biol. Chem.* (2018).
- 588 35. Grell, T.A., Goldman, P.J. & Drennan, C.L. SPASM and twitch domains in S-
589 adenosylmethionine (SAM) radical enzymes. *J. Biol. Chem.* **290**, 3964-71 (2015).
- 590 36. Broderick, J.B., Duffus, B.R., Duschene, K.S. & Shepard, E.M. Radical S-adenosylmethionine
591 enzymes. *Chem Rev* **114**, 4229-317 (2014).
- 592 37. Tao, L., Zhu, W., Klinman, J.P. & Britt, R.D. Electron Paramagnetic Resonance Spectroscopic
593 Identification of the Fe-S Clusters in the SPASM Domain-Containing Radical SAM Enzyme
594 PqqE. *Biochemistry* **58**, 5173-5187 (2019).
- 595 38. Zhu, W. et al. Structural Properties and Catalytic Implications of the SPASM Domain Iron-
596 Sulfur Clusters in *Methylorubrum extorquens* PqqE. *J Am Chem Soc* **142**, 12620-12634 (2020).
- 597 39. Yokoyama, K., Ohmori, D., Kudo, F. & Eguchi, T. Mechanistic study on the reaction of a radical
598 SAM dehydrogenase BtrN by electron paramagnetic resonance spectroscopy. *Biochemistry* **47**,
599 8950-60 (2008).
- 600 40. Blaszczyk, A.J. et al. Spectroscopic and Electrochemical Characterization of the Iron-Sulfur
601 and Cobalamin Cofactors of TsrM, an Unusual Radical S-Adenosylmethionine Methylase. *J Am*
602 *Chem Soc* **138**, 3416-26 (2016).
- 603 41. Weerasinghe, N.W., Habibi, Y., Uggowitz, K.A. & Thibodeaux, C.J. Exploring the
604 Conformational Landscape of a Lanthipeptide Synthetase Using Native Mass Spectrometry.
605 *Biochemistry* **60**, 1506-1519 (2021).
- 606 42. Benjdia, A. et al. Thioether bond formation by SPASM domain radical SAM enzymes: C α
607 H-atom abstraction in subtilosin A biosynthesis. *Chem Commun (Camb)* **52**, 6249-6252 (2016).
- 608 43. Morinaka, B.I. et al. Radical S-adenosyl methionine epimerases: regioselective introduction of
609 diverse D-amino acid patterns into peptide natural products. *Angew Chem Int Ed Engl* **53**, 8503-
610 7 (2014).
- 611 44. Dathe, M. & Wieprecht, T. Structural features of helical antimicrobial peptides: their potential
612 to modulate activity on model membranes and biological cells. *Biochim Biophys Acta* **1462**, 71-
613 87 (1999).

- 614 45. Ayikpoe, R. et al. Spectroscopic and Electrochemical Characterization of the Mycofactocin
615 Biosynthetic Protein, MftC, Provides Insight into Its Redox Flipping Mechanism. *Biochemistry*
616 **58**, 940-950 (2019).
- 617 46. Balo, A.R. et al. Trapping a cross-linked lysine-tryptophan radical in the catalytic cycle of the
618 radical SAM enzyme SuiB. *Proc Natl Acad Sci U S A* **118**(2021).
- 619 47. Brito, J.A., Denkmann, K., Pereira, I.A., Archer, M. & Dahl, C. Thiosulfate dehydrogenase
620 (TsdA) from *Allochromatium vinosum*: structural and functional insights into thiosulfate
621 oxidation. *J Biol Chem* **290**, 9222-38 (2015).
- 622 48. Nakamura, R., Hikita, M., Ogawa, S., Takahashi, Y. & Fujishiro, T. Snapshots of PLP-substrate
623 and PLP-product external aldimines as intermediates in two types of cysteine desulfurase
624 enzymes. *FEBS J* **287**, 1138-1154 (2020).
- 625 49. Denisov, I.G., Makris, T.M., Sligar, S.G. & Schlichting, I. Structure and chemistry of
626 cytochrome P450. *Chem Rev* **105**, 2253-77 (2005).
- 627 50. Kudo, F., Hoshi, S., Kawashima, T., Kamachi, T. & Eguchi, T. Characterization of a radical S-
628 adenosyl-L-methionine epimerase, NeoN, in the last step of neomycin B biosynthesis. *J Am*
629 *Chem Soc* **136**, 13909-15 (2014).
- 630 51. Besandre, R.A. et al. HygY Is a Twitch Radical SAM Epimerase with Latent Dehydrogenase
631 Activity Revealed upon Mutation of a Single Cysteine Residue. *J Am Chem Soc* **143**, 15152-
632 15158 (2021).
- 633 52. Dong, S.H., Liu, A., Mahanta, N., Mitchell, D.A. & Nair, S.K. Mechanistic Basis for Ribosomal
634 Peptide Backbone Modifications. *ACS Cent Sci* **5**, 842-851 (2019).
- 635 53. Zhao, G. et al. Structural Basis for a Dual Function ATP Grasp Ligase That Installs Single and
636 Bicyclic omega-Ester Macrocycles in a New Multicore RiPP Natural Product. *J Am Chem Soc*
637 **143**, 8056-8068 (2021).
- 638 54. Song, I. et al. Molecular mechanism underlying substrate recognition of the peptide
639 macrocyclase PsnB. *Nat Chem Biol* **17**, 1123-1131 (2021).
- 640 55. Miller, F.S. et al. Conformational rearrangements enable iterative backbone N-methylation in
641 RiPP biosynthesis. *Nat Commun* **12**, 5355 (2021).
- 642 56. Fyfe, C.D. et al. Crystallographic snapshots of a B12-dependent radical SAM methyltransferase.
643 *Nature* **602**, 336-342 (2022).
- 644 57. Krissinel, E. & Henrick, K. Inference of macromolecular assemblies from crystalline state. *J*
645 *Mol Biol* **372**, 774-97 (2007).

646

647

648 **Methods**

649 **Cloning of EpeE D210A and Y2F-Y209F mutants**

650 The EpeE tyrosine mutants were obtained by site-directed mutagenesis with the plasmid pET28-Strep-TEV-EpeE used as DNA
651 template. To generate the Y2F-Y209F mutant the following primers were used: 5'-CAT ATG TTC AAC AAA ACC GTG
652 AGC-3' ; 5'-TCC GGG TTT CGA TAT TGT GTA TCA TC-3' ; 5'-ACA ATA TCG AAA CCC GGA CAA TGC AG-3'.
653 PCR reactions typically contained 1 μ M of each primer, 250 μ M of each dNTP, 1 μ l of High Fidelity Polymerase (Thermo),
654 ~50 ng DNA template and performed using the following PCR cycling parameters: 1 cycle at 95°C for 2 min followed by 36
655 cycles of 95°C for 30 sec (denaturation), 55-60°C for 30 sec (hybridation), 72°C for 90 s (extension) and 1 cycle at 72°C for
656 10 min. PCR products were purified on 1-2% agarose gel, digested with NdeI and XhoI (NEB), purified and ligated into
657 NdeI/XhoI digested pET28-Strep-TEV plasmid. The D210A mutant gene was synthesis by GeneCust and ligated in plasmid
658 pET28. The ligation products were transformed into chemically competent *E. coli* BL21 (DE3) star strain. Clones were selected
659 on LB agar plate containing 50 μ g.mL⁻¹ kanamycine. One clone was selected after we checked the sequence of the targeted
660 gene by DNA sequencing.

661

662 **Protein purification**

663 The constructs of wild-type and C223A mutant streptavidin-tagged EpeE were the same as previously published⁹. All
664 recombinant proteins were overexpressed and purified as follows. Typically, 9 L of *E. coli* BL21 cells transformed with pET28
665 plasmid containing the construct were grown in Luria-Broth (LB) media at 37°C with 50 μ g/mL Kanamycin, and protein
666 expression induced at Abs_{600nm} ~ 0.6 with 700 μ M IPTG. Overexpression was conducted overnight and cells resuspended in
667 Buffer A (500 mM NaCl, 50 mM TrisHCl, pH 8.0) containing 0.5% Triton X-100, protease inhibitors and sonicated for 4 min
668 on ice. Cell debris were pelleted by ultracentrifugation at 45,000 g (Beckman coulter) before loading supernatant on Streptactin
669 resin (IBA) equilibrated in buffer A. After washing in buffer A, the recombinant protein was eluted with buffer A supplemented
670 by 3 mM desthiobiotin. Protein was aliquoted, flash frozen in liquid N₂ and stored at -80°C. Concentration was measured by
671 absorbance at 280 (using ProtParam calculated ϵ and molecular weights) and purity assessed by SDS-PAGE on 12% gels and
672 PageBlue staining.

673

674 **Iron sulfur clusters reconstitution**

675 *In vitro* reconstitution of the EpeE [4Fe-4S] clusters was achieved in presence of 3 mM DTT by addition of 8 molar excess of
676 (NH₄)₂Fe(SO₄)₂ and Na₂S. After incubation under anaerobic atmosphere, excess of unbound iron and sulfur was removed onto
677 a desalting column against buffer A with 3 mM DTT. Reconstitution of the protein was verified by recording UV-visible spectra
678 (250-700 nm).

679

680 **Peptide synthesis**

681 The EpeX peptide **1** and RiPP-fragments peptide **2** (KKEITNNETVKNLEFKGLLDESQKLAKVNDL), peptide **3**
682 (KNLEFKGLLDESQKLAKVNDL), peptide **4** (WYFVKSKEN), peptide **5** (FVKSKENRWIL), peptide **6**
683 (KENRWILGSGH), peptide **7** (NRWILGSGH) were synthesized by solid-phase synthesis (ProteoGenix, France). In bold,
684 residues targeted by EpeE.

685

686 **EPR analysis**

687 EPR samples were prepared immediately after reconstitution of the iron-sulfur clusters in the glove box. Reduction was
688 achieved in 5 minutes by the addition of 3 mM sodium dithionite. Samples in the presence of SAM were prepared by addition
689 of 3-5 fold stoichiometric excess of SAM. Samples were then frozen in liquid isopentane in the glove box and then maintained
690 in liquid nitrogen until EPR measurements were performed. EPR spectra were recorded on a Bruker ElexSys-500 X-band
691 spectrometer equipped with a standard rectangular cavity (ST4102) fitted to an Oxford Instruments liquid helium cryostat
692 (ESR900) and temperature control system. The spectrometer settings were as follows: microwave frequency, 9.48 GHz,
693 conversion time of 80 ms, modulation amplitude of 1 mT, and modulation frequency of 100 kHz. Other settings are given in
694 the corresponding figure captions.

695 HYSCORE experiments were measured at 6 K using a Bruker EleXsys E580 spectrometer equipped with an ER4118X-MD5
696 dielectric resonator and an Oxford Instruments CF 935 cryostat. This four-pulse experiment ($\pi/2$ - τ - $\pi/2$ - t_1 - π - t_2 - $\pi/2$ - τ -echo) was
697 employed with an appropriate 8 step phase-cycling scheme to eliminate unwanted features from the experimental electron spin
698 echo envelopes. The intensity of the echo after the fourth pulse was integrated over 32 ns with varied t_2 and t_1 and constant τ .
699 The length of a $\pi/2$ pulse was 12 ns and of a π pulse 24 ns. A τ value of 132 ns and a shot repetition rate of 1 kHz were used.
700 HYSCORE data were collected in the form of 2D time-domain patterns containing 256 \times 256 points with steps of 16 ns. Spectra
701 were recorded at the magnetic field value corresponding to the maximum absorption of the [4Fe-4S]¹⁺ signal in the absence of
702 SAM (corresponding to $g = 1.929$). HYSCORE spectra were processed using Bruker's Xepr software. Relaxation decays were
703 subtracted (fitting by 3rd order polynomial functions) followed by zero-filling to 1024 points and tapering with a Hamming
704 window, before 2D Fourier transformation which finally gives the spectrum in frequency domain. Processed data were then
705 imported into Matlab (The MathWorks Inc., Natick, MA) for plotting. HYSCORE spectra are shown in absolute value mode
706 and are presented as contour plots.

707

708 **Enzyme assay**

709 The activity of EpeE towards the synthetic peptides was assayed in deuterated buffer (150 mM KCl, 25 mM TrisDCl, pH 8.0,
710 DTT 3 mM); all compounds were dissolved in D₂O and the reconstituted protein was buffer exchanged against deuterated
711 buffer. EpeE (235 μ M) was incubated with 3 mM DTT, 3 mM SAM and 2.25 mM peptide. The reactions were initiated by
712 addition of 3 mM sodium dithionite.

713 For the kinetic experiments, the EpeE WT, C223A, D210A and Y2F-Y209F mutants (100 μ M) were incubated with 1 mM
714 SAM, 500 μ M peptide 6 and reactions were initiated with the addition of flavodoxin/flavodoxin reductase and 2.7 mM NADPH.
715 All reactions were performed at 25°C and 15 μ L aliquots sampled overtime for LC-MS/MS analysis.
716

717 **Liquid chromatography–mass spectrometry/mass spectrometry analysis**

718 LC-MS/MS analysis were achieved using a Q-Exactive Focus mass spectrometer (ThermoFisher Scientific) with the HESI2
719 electrospray ion source associated to a Vanquish Flex LC system (Thermo Fisher Scientific). Molecule separation was
720 performed on a Zorbax Eclipse Plus C18 column (2.1X50mm, 1.8 μ m, RRHT, Agilent). Samples were dilute one hundred time
721 before injection with TFA 0.1% or in acetonitrile 50%, to discard the protein by precipitation. Peptides 4, 5, 6 or 7 were eluted
722 on the reverse phase column by an acetonitrile gradient with formic acid 0.1% as ion pairing agent and detected by mass
723 spectrometry in positive mode. The doubly charged ions corresponding to the peptides 4, 5, 6, 7 were selected for HCD
724 fragmentation step at 35 % or 20 % of NCE. For detection and quantitation of the epimerized peptide 5 by mass spectrometry,
725 the samples were hydrolyzed using trypsin Promega (V5111) to produce the peptide fragment WILGSGH and extract the
726 corresponding MS signal of the doubly charge ion (385.21²⁺). This method enables us to quantify the epimerized and
727 unmodified peptides. Unmodified peptide fragment eluted at 13.7 min and the epimerized fragment at 18.2 min from the
728 column. The 5'-dA produced during *in vitro* reactions with EpeE (wild-type and D210A, C223A and Y2F-Y209F mutants) was
729 quantified in the sample by mass spectrometry using a direct standard curve of 5'-dA.
730

731 **Crystallization of EpeE, EpeE C223A, EpeE D210A mutants and complexes with peptides 5 and 6**

732 For crystallization purposes, the freshly reconstituted protein was further purified by size exclusion on a Superdex-200 10/300
733 GL Increase column (Äkta system, GE Healthcare) to achieve homogeneity in the protein preparation. Protein was then
734 typically concentrated to 20 mg/mL before setting up crystallization experiments. Crystals were obtained by using the sitting
735 drop vapor diffusion technique at 21°C under anaerobic atmosphere. After several rounds of optimization, brown rod shaped
736 single crystals were obtained in 3 % Ethylene Glycol, 9.6 % PEG 8,000, 0.1 M HEPES pH 7.5, with a 2:1 protein:mother liquor
737 ratio, and were used for anomalous data collection (**EpeE phasing dataset, Extended Table 1**). EpeE wild-type crystals (**EpeE**
738 **WT, Extended Table 1**) appeared within 24 h by using hanging drop diffusion and a 1:1 mixing of protein (7.5 mg ml⁻¹ with
739 0.5 mM SAH) and precipitant solution (0.1 M Tris-HCl pH 8.5, 17.5 % polyethylene glycol (PEG) 1,000). EpeE D210A mutant
740 crystals (**EpeE D210A, Extended Table 1**) were grown in same conditions as EpeE WT in presence of SAH. EpeE C223A
741 mutant crystals (**EpeE C223A, Extended Table 1**) were grown in 2:1 drops mixing protein (10 mg ml⁻¹ with 1 mM SAM) and
742 precipitant solution. The crystals of complexes from EpeE wild-type (**EpeE WT peptide 5, Extended Table 1**) and EpeE
743 C223A mutant (**EpeE C223A peptide 5, EpeE C223A peptide 6, Extended Table 1**) were obtained mixing precipitants (0.1
744 M Tris-HCl pH 8.5, 14-20% PEG 1,000) with protein, SAH (0.5 mM) and peptide (5 mM). All crystals were typically obtained
745 within 24 hours under anaerobic atmosphere and flash cooled in liquid N₂ under anaerobic conditions.
746

747 **Crystallographic structure determinations**

748 X-ray diffraction data were recorded on PROXIMA-1 beamline at Synchrotron SOLEIL⁵⁸, equipped with a Pilatus-6M hybrid
749 pixel detector⁵⁹ and a three-axis SmarGon goniometer. An X-ray energy of 7.14 keV was chosen for the single anomalous
750 phasing experiments, for which two sets of images were recorded at two different Chi angles to favor obtaining a more complete
751 merged data at 2.99 Å resolution. The X-ray energy was 12.67 keV for subsequent data collection. For the experimental phasing
752 measurements, the X-ray energy was attenuated to 5% of the beam intensity, providing with a flux of 1.0 x 10¹⁰ photons.s⁻¹
753 at the sample position; the more standard data at 12.67 keV were recorded with 20% of the beam intensity. Phasing and data
754 analysis and processing was performed using SHARP/AutoSHARP (SHARP 2.8.12 and Sushi 3.10.11), and the CCP4 suite
755 (7.1.016). Data were processed with XDS 2022/01/10⁶⁰ through the *xdsme* scripting package⁶¹. The (hkl) and (-h-k-l)
756 reflections were treated separately in all steps, including scaling and merging. Data sets were scaled with XSCALE
757 2022/01/10⁶⁰, converted to MTZ format with POINTLESS 1.12.13⁶² and merged with AIMLESS 0.7.8⁶³, as implemented within
758 the *xdsme* automated procedure.

759 For the EpeE phasing dataset, structure-factor amplitudes were obtained with TRUNCATE 8.0.010⁶⁴. The Matthews coefficient
760 suggested that the crystal contained two monomers *per* asymmetric unit. Four iron cluster sites were located with SHELXC/D
761 2016/1⁶⁵, and their respective positions were refined with SHELXE 2019/1 (through HKL2MAP)⁶⁶ and Phaser 2.8⁶⁷. Initial
762 correct substructures were determined immediately with SHELXD 2013/2, with two well-separated clusters in the plot of CC_{all}
763 versus CC_{weak}. The phase information was improved using the existing non-crystallographic symmetry (NCS) between the two
764 molecules within the asymmetric unit. One helix surrounding the iron clusters was docked in the original electron density using
765 Coot⁶⁸ to facilitate the calculation of the matrix. Given this matrix, Phaser unequivocally identified the rotation and translation
766 parameters of two monomers and confirmed the space group P2₁2₁2₁. Side chains were placed by automated model building
767 with Buccaneer 1.6.12/REFMAC5⁶⁹. Missing residues, water molecules and ligands were fitted in the 2F_o-F_c and F_o-F_c
768 electron-density maps using Coot. For structure refinements of the subsequent models, phases were introduced from the original
769 structure as a template coordinates (Phaser) and the structures were refined iteratively with REFMAC5 or BUSTER (version
770 2.10.4)⁷⁰. Manual building was performed with Coot (version 0.9.6.1.1). The structures were validated by MolProbity as
771 implemented in phenix version 1.19.2-4158⁷¹. Data collection and refinement statistics are shown in Extended Table 1. All
772 structural representations were generated with PyMOL v0.99 (DeLano Scientific LLC) or PyMOL v2.5 (Schrödinger, LLC).
773

774 **SEC-SAXS data measurement**

775 All the data was collected in SEC-SAXS mode with an in-line Superdex 200 Increase 5/150 GL column (GE Healthcare).
776 Homogeneous reconstituted proteins were loaded on our anaerobic setup which was based on an HPLC system equilibrated
777 with degassed buffer containing 1 mM DTT and an auto-sampler flushed by a continuous flux of N₂. The SAXS data was
778 collected at the SWING beamline at the SOLEIL synchrotron, France, equipped with an Eiger 4M detector with a sample-to-

779 detector distance of 2 m². The parameters used for SAXS data collection are given in **Supplementary Table 10**. More
780 information is available in **Supplementary Table 10**.

781

782 **Reporting summary**

783 Further information on research design is available in the Nature Research Reporting Summary linked to this paper.

784 **Data Availability**

785 Atomic coordinates and structure factors for the reported crystal structures in this work have been deposited in the Protein Data
786 Bank upon accession codes: 8AI1, 8AI2, 8AI3, 8AI4, 8AI5 & 8AI6. SAXS data have been deposited in the Small Angle
787 Scattering Biological Data Bank upon accession codes SASDRS7, SASDRR7. The data for this study are available within the
788 paper and its Supplementary Information. Source data are provided with this paper.

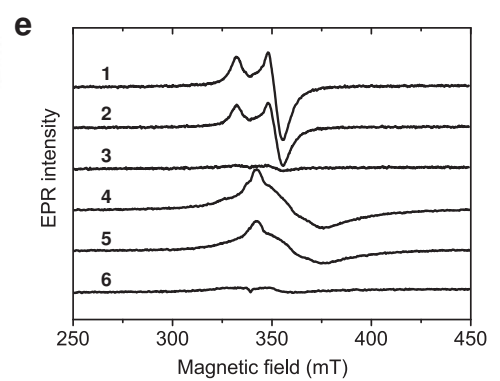
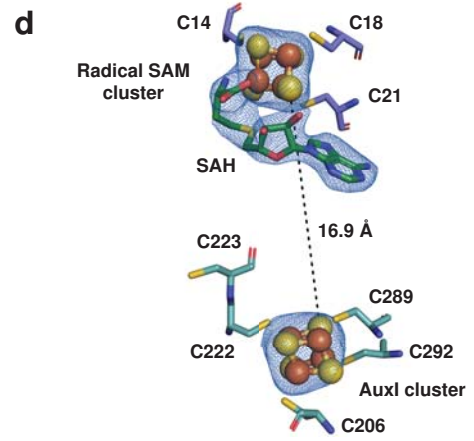
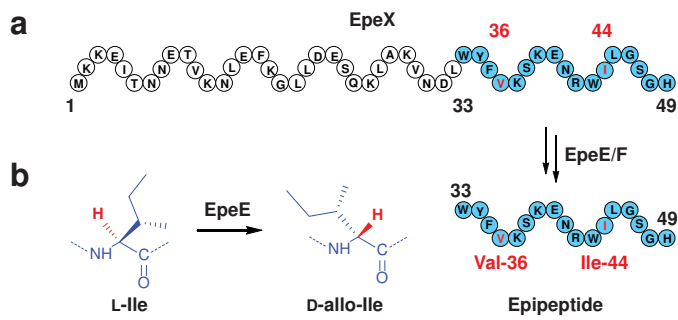
789

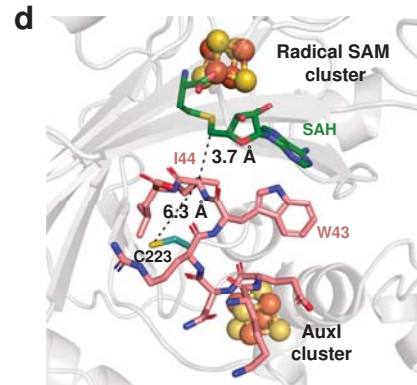
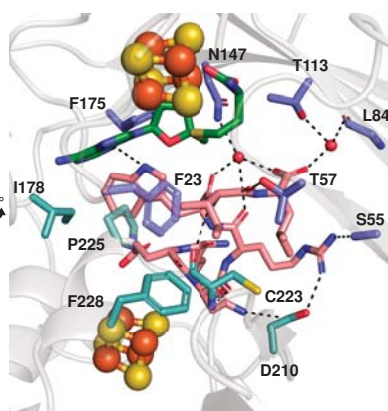
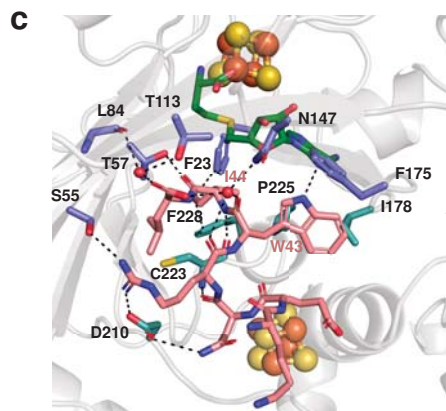
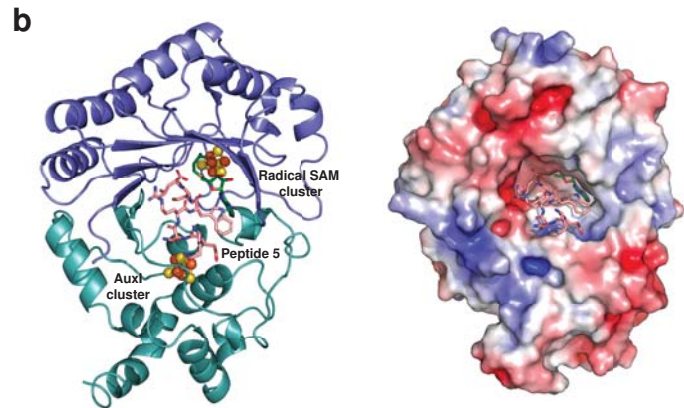
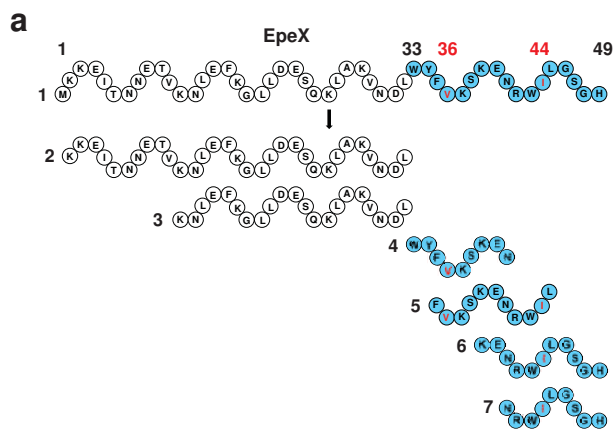
790 **References**

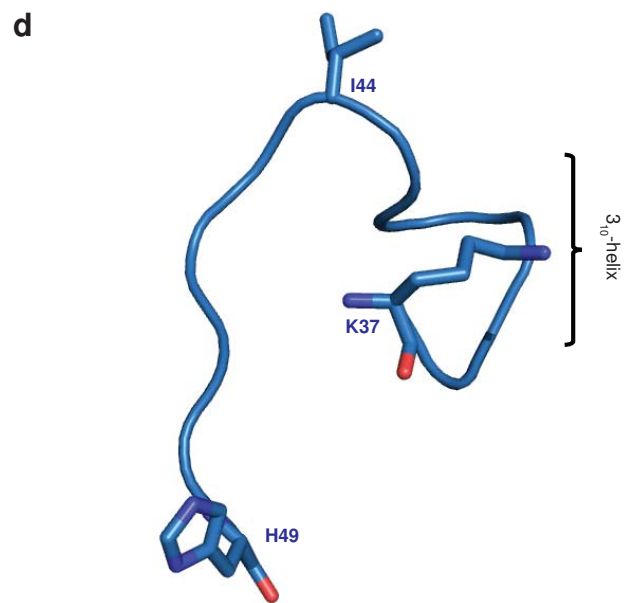
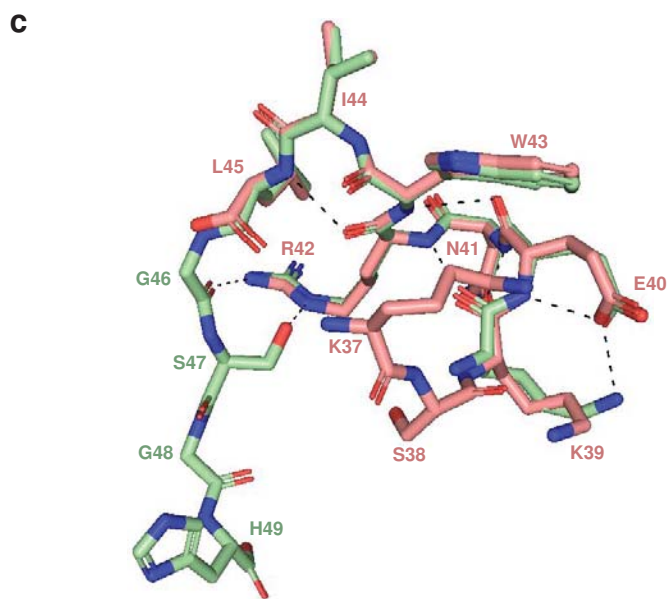
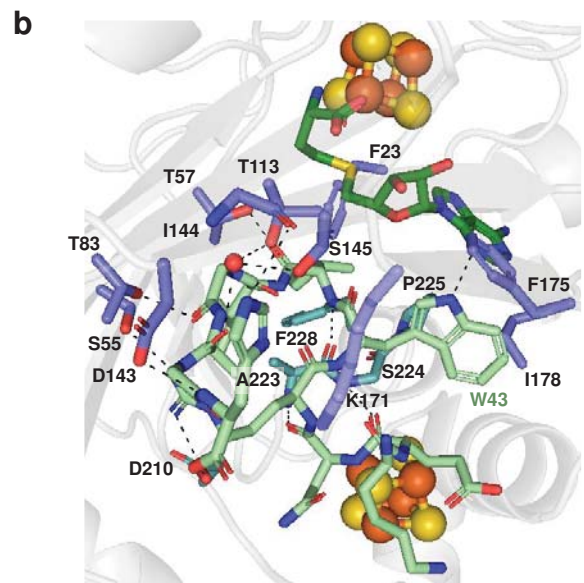
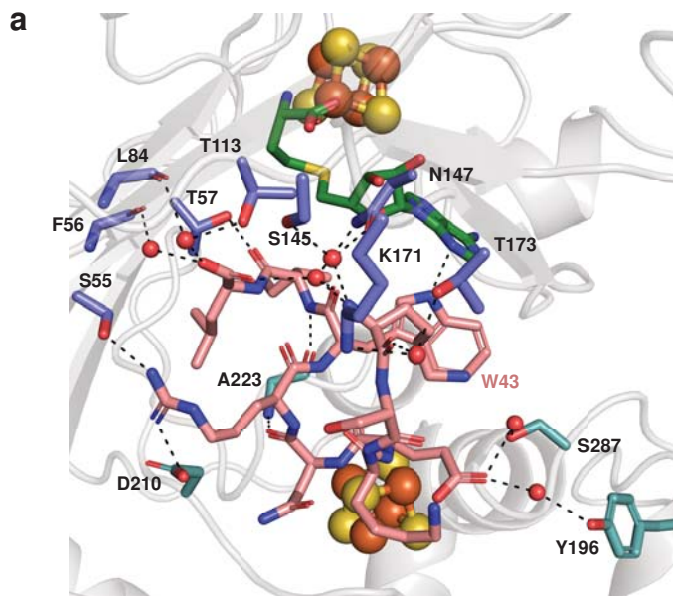
791

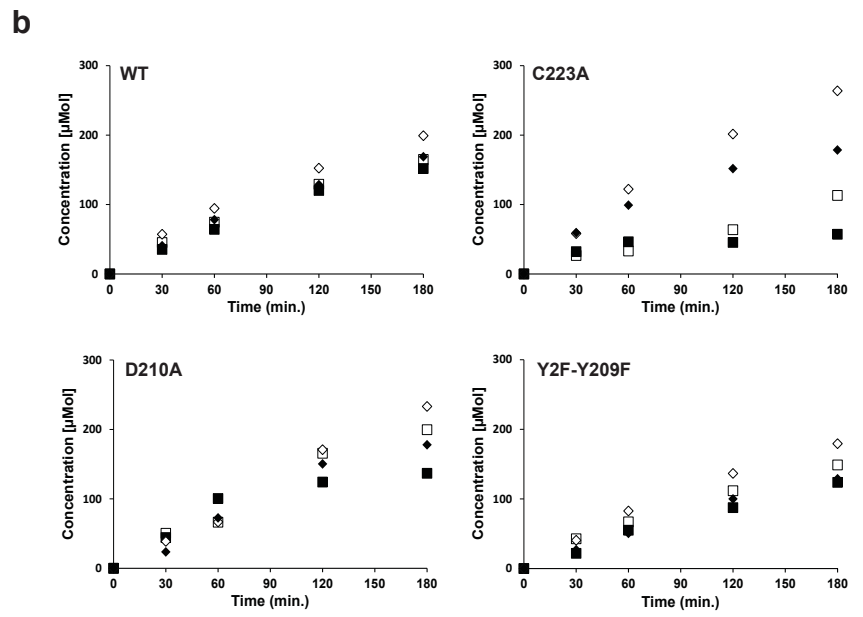
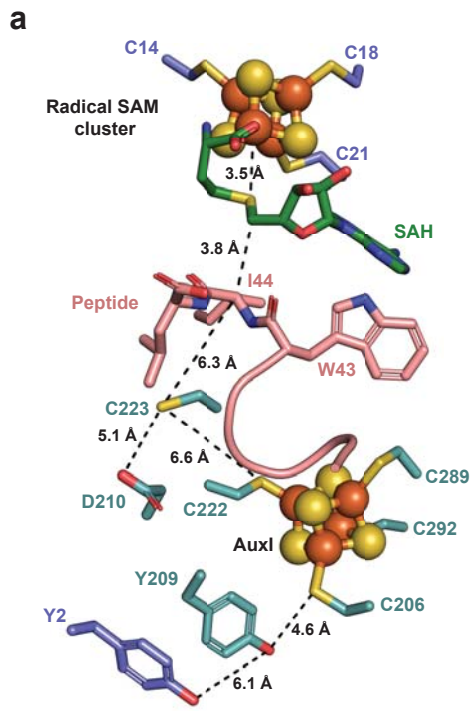
- 792 58. Coati, A. et al. Status of the crystallography beamlines at synchrotron SOLEIL*. *The European Physical Journal Plus*
793 **132**(2017).
- 794 59. Kraft, P. et al. Performance of single-photon-counting PILATUS detector modules. *Journal of Synchrotron Radiation*
795 **16**, 368-375 (2009).
- 796 60. Kabsch, W. XDS. *Acta Crystallographica Section D Biological Crystallography* **66**, 125-132 (2010).
- 797 61. Legrand, p. XDSME: XDS Made Easier. GitHub repository (2017).
- 798 62. Evans, P. Scaling and assessment of data quality. *Acta Crystallographica Section D Biological Crystallography* **62**, 72-
799 82 (2006).
- 800 63. Evans, P.R. & Murshudov, G.N. How good are my data and what is the resolution? *Acta Crystallographica Section D*
801 *Biological Crystallography* **69**, 1204-1214 (2013).
- 802 64. Winn, M.D. et al. Overview of the CCP 4 suite and current developments. *Acta Crystallographica Section D Biological*
803 *Crystallography* **67**, 235-242 (2011).
- 804 65. Sheldrick, G.M. A short history of SHELX. *Acta Crystallogr A* **64**, 112-22 (2008).
- 805 66. Pape, T. & Schneider, T.R. HKL2MAP : a graphical user interface for macromolecular phasing with SHELX programs.
806 *Journal of Applied Crystallography* **37**, 843-844 (2004).
- 807 67. McCoy, A.J. et al. Phaser crystallographic software. *Journal of Applied Crystallography* **40**, 658-674 (2007).
- 808 68. Emsley, P., Lohkamp, B., Scott, W.G. & Cowtan, K. Features and development of Coot. *Acta Crystallographica Section*
809 *D Biological Crystallography* **66**, 486-501 (2010).
- 810 69. Murshudov, G.N. et al. REFMAC 5 for the refinement of macromolecular crystal structures. *Acta Crystallographica*
811 *Section D Biological Crystallography* **67**, 355-367 (2011).
- 812 70. Smart, O.S. et al. Exploiting structure similarity in refinement: automated NCS and target-structure restraints in BUSTER.
813 *Acta Crystallographica Section D Biological Crystallography* **68**, 368-380 (2012).
- 814 71. Chen, V.B. et al. MolProbity : all-atom structure validation for macromolecular crystallography. *Acta Crystallographica*
815 *Section D Biological Crystallography* **66**, 12-21 (2010).
- 816 72. Thureau, A., Roblin, P. & Perez, J. BioSAXS on the SWING beamline at Synchrotron SOLEIL. *Journal of Applied*
817 *Crystallography* **54**, 1698-1710 (2021).

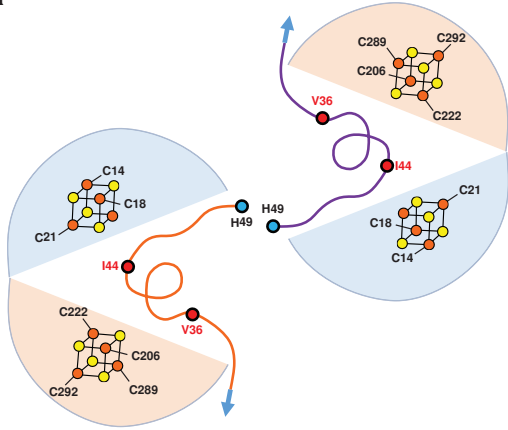
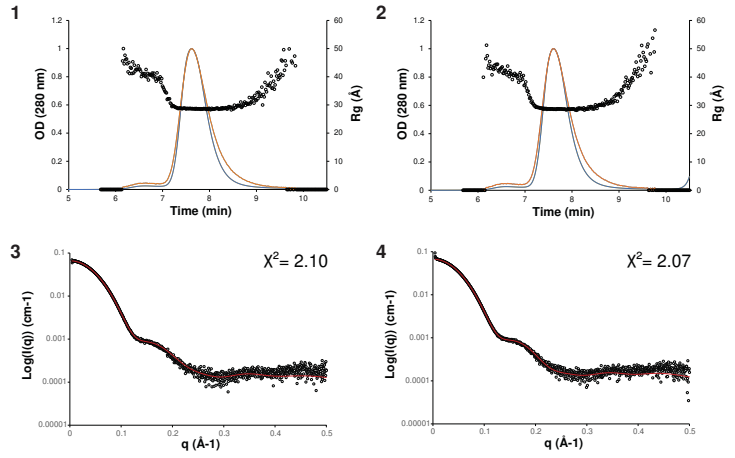
818









a**b****c**